



1 Article

2 Gas-Phase Formation of Highly Luminescent 2D

GaSe Nanoparticle Ensembles in a Nonequilibrium

4 Laser Ablation Process

- 5 Salah Elafandi ¹, Zabihollah Ahmadi ¹, Nurul Azam ¹ and Masoud Mahjouri-Samani ^{1,*}
- Department of Electrical and Computer Engineering, Auburn University, Auburn, AL, USA; e-mail@e-mail.com
- * Correspondence: mahjouri@auburn.edu
- 9 Received: date; Accepted: date; Published: date

Abstract: Interest in layered two-dimensional (2D) materials has been escalating rapidly over the past few decades due to their promising optoelectronic and photonic properties emerging from their atomically-thin 2D structural confinements. When these 2D materials are further confined in lateral dimensions toward zero-dimensional (0D) structures, 2D nanoparticles and quantum dots with new properties can be formed. Here, we report a nonequilibrium gas-phase synthesis method for the stoichiometric formation of gallium selenide (GaSe) nanoparticles ensembles that can potentially serve as quantum dots. We show that the laser ablation of a target in an argon background gas condenses the laser-generated plume resulting in the formation of metastable nanoparticles in the gas phase. The deposition of these nanoparticles onto the substrates results in the formation of nanoparticle ensembles, which are then post-processed to crystallize or sinter the nanoparticles. The effects of background gas pressures, in addition to crystallization/sintering temperatures, are systematically studied. Scanning electron microscopy (SEM), photoluminescence (PL) spectroscopy, and time-correlated single-photon counting (TCSPC) measurement are used to study the correlations between growth parameters, morphology, and optical properties of fabricated 2D nanoparticle ensembles.

Keywords: 2D materials, 2D nanoparticles, 2D quantum dots, Laser ablation, Laser-based synthesis.

1. Introduction

During the past decade, a large family of two-dimensional (2D) materials beyond graphene have been under intense investigation.[1-3] Examples of such 2D layered structures include hexagonal boron nitride (hBN),[4] metal chalcogenides (MCs: e.g., GaSe, InS)[5] and transition metal dichalcogenides (TMDCs: e.g., MoS₂, WSe₂).[6-7] These 2D materials family offer a broad range of remarkable electrical,[7-9] optical,[10] chemical,[11] and mechanical properties[12] that are often originated from their structural and quantum confinement to 2D plane.[13-15] In general, 2D materials are an appealing group of materials to substitute or complement traditional 3D electronic and optoelectronic materials.[16-18]

When these 2D materials are additionally confined in the lateral dimensions, zero-dimensional (0D) nanoparticles can be formed, mimicking the potential properties of quantum dots (QDs).[19-21] These 2D nanoparticles show improved or new properties in addition to the inherent properties of their parent 2D materials.[22-23] Low-toxicity,[24] higher specific surface area,[25-26] tunable luminescence,[27-29] improved dispersibility in both aqueous and nonaqueous solvents,[30-31] ability to hybridize with other nanomaterials,[32-33] in addition to doping and functionalization flexibility[34-35] are few of the advantages exhibited by such 2D nanoparticles. Therefore, they are strong candidates for electronic,[36] optical,[33] energy,[4] biomedical,[28] sensing,[23] and

catalytic[37] applications. Ultrasonication-based,[38-39] especially the ones accompanied by solvothermal treatments,[40-41] syntheses methods have been widely adopted to produce 2D nanoparticles due to their low-toxicity and ability to maintain the intrinsic properties of 2D bulk crystals.[42] These techniques are, however, time-consuming with low quantum yield, production yield, and repeatability.[42] To address such lengthy processes, femtosecond laser ablation in the aqueous environment has been introduced[43-44] that showed great promise as a fast and green approach to fabricate and functionalize 2D QDs. [35,45] Another effective method to obtain large-scale monolayer QDs is intercalation-assisted exfoliation[36,46]. This method could, however, lead to phase transition[47] and contamination.[48] Electrochemical synthesis[49-50] is another low-cost technique but with better reproducibility. In general, these methods lack compositional tunability as well as compatibility with the direct deposition and digital formation of hybrid materials and heterostructures.

Among 2D materials, gallium selenide (GaSe) is a direct bandgap material (~2.2 eV) in its bulk form that has D_{3h} symmetry with a lattice constant of 0.374 nm.[51] In 1996, Stoll et al. obtained "strings of pearls" shaped GaSe nanoparticles with a mean diameter of 42 nm through metal-organic chemical vapor deposition (MOCVD) synthesis process.[52] The colloidal GaSe was obtained a year later by Allakhverdiev et al, through ultrasonication of bulk GaSe crystal in methanol.[53] Moreover, in 2001, Chikan and Kelly obtained highly confined and luminescent surface capped GaSe nanoparticles using high-temperature inorganic synthesis and column chromatography.[54] In recent years, the high-pressure pulsed laser deposition (PLD) process has shown the ability to form metastable nanoparticles in the gas phase.[55] For instance, Mahjouri-Samani et al., have recently reported the formation of various metastable nanoparticle and nanosheets using a high-pressure PLD process.[56] Dai et al. have also reported the deposition of CdSe QDs on Zn₂SnO₄ nanowires by PLD.[57]

Here, we report a solution-free, fast, and effective laser-based approach to synthesize highly luminescent 2D GaSe nanoparticle ensembles. The pulsed laser ablation/deposition (PLA/PLD) method is used as a versatile method to ablate a bulk GaSe target and form a stoichiometric plume (see Supporting Information). Condensation of this plume in background argon gas pressure allows tuning the formation of aggregates and nanoparticles in gas-phase. Our approach simplifies the complexity of existing methods through the elimination of slow and uncontrolled chemical reactions. Also, this method has the potential of forming tunable nanoparticles heterostructures by alternating the ablation target during the deposition. Scanning electron microscopy (SEM), photoluminescence (PL) spectroscopy, and time-correlated single-photon counting (TCSPC) spectroscopy were used to study the correlations between growth parameters, morphology, and optical properties of fabricated structures.

2. Materials and Methods

The pulsed laser ablation/deposition experiments in this study were performed in a 21-inch spherical vacuum chamber. Si/SiO₂ substrates (2×2 cm) were placed at the tip of the plume and parallel to the target. An excimer laser (CompexPro KrF 248nm wavelength with 20 ns pulse duration) was used to ablate a rotating bulk GaSe target in order to generate GaSe nanoparticles and deposit them onto the Si/SiO₂ substrates. The target was irradiated at a 45° angle of incidence with repetition rates of 2 Hz. The laser repetition rate of 2 Hz was chosen to allow enough time for the generated plume to clear before the next plume arrives in order to minimize the effect of plume-plume collisions. Laser energy of 300 mJ with a 2×5mm beam size (i.e., 3 Jcm⁻²) on the target was used to ensure the stoichiometric transfer of materials. The substrate to target distance was adjusted to be a few millimeters above the visible laser plume to ensure the collection of pure nanoparticles on the substrates. The deposition was up to 5000 pulses to collect an adequate amount of nanoparticles for subsequent characterizations.

The ensemble nanoparticles were heat-treated using a 3-inch diameter 3-zone tube furnace. The nanoparticle deposited on the Si/SiO₂ substrates were placed inside a ceramic boat and entered into the center zone of the tube furnace. The tube was first pumped down to a few millitorrs. Before

heating, the pressure was increased to atmospheric pressure by flowing an argon gas into the tube. During the heating process, 100 sccm Ar gas was continuously flowing through the quartz tube. The samples were treated under various temperatures ranging from 200 to 500 °C. After heating, the furnace was turned off, and the substrates were cooled down to room temperature while the Ar gas was flowing.

Photoluminescence spectroscopy and lifetime measurements were performed in a custom-made optical spectroscopy system capable of measuring PL and PL lifetime. The PL measurements were performed using a 50x objective lens (NA = 0.75). A Horiba HR spectrometer with a 300 g/mm grating was used for PL. A picosecond 405 nm lasers and a continuous-wave 532 nm laser were used as excitation sources. The laser power was minimized to avoid potential beam-induced alteration of the nanoparticles during the measurements. Lifetime measurements were performed using a Horiba TCSPC system with a picosecond 405 nm laser as the excitation source. The number of counts was limited to 1000 counts in order to avoid potential beam-induced damage or alteration of the nanoparticles. Horiba EzTime Software was used to collect and analyze the lifetime measurement data.

A high-resolution Zeiss EVO 50 variable pressure SEM attached to Oxford Instruments INCA spectrometer for energy-dispersive x-ray spectroscopy (EDX) was used to characterize the morphology and structural composition of the deposited nanoparticles. SEM images were obtained with 10 kV accelerating voltage, while EDX was performed using 20 kV. The EDX data was analyzed using Oxford INCA software. For transmission electron microscopy (TEM) imaging, a Zeiss EM10 transmission electron microscope with an accelerating voltage of 60 kV was used for single-particle and aggregation analysis. The TEM grids were prepared by first sonicating the nanoparticles in ethanol for 1 minute, followed by steering the TEM grids inside the solution to collect the nanoparticles.

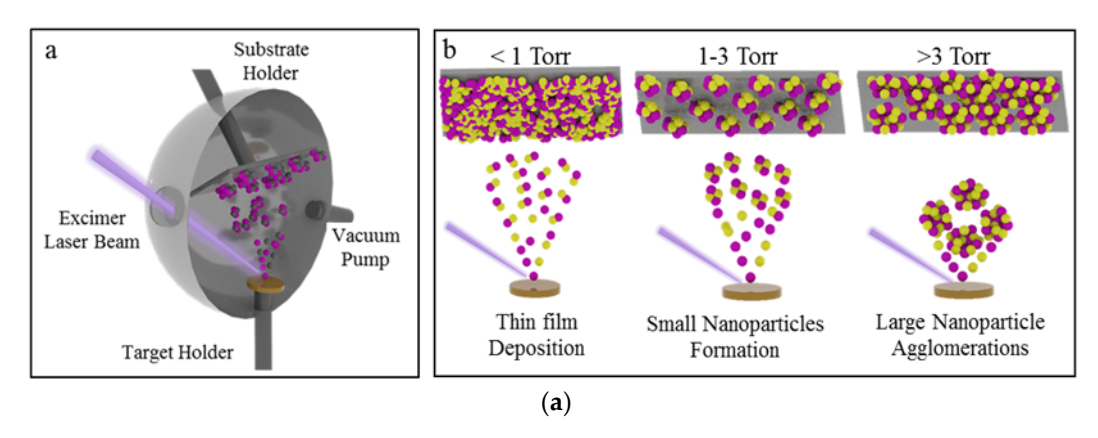


Figure 1. Schematic illustration of the experimental setup used for the formation and assembly of the 2D nanoparticles in this study (a). Schematic illustration of the laser-generated plume dynamic and evolution of nanoparticle formation as a function of background pressure (b).

3. Results and discussion

Typically, the PLD process (Figure 1a) involves the formation of a forward-directed laser-plasma consisting of fast ions and neutral atoms followed by slower-moving molecules and clusters.[51] For instance, the ablation of a target in vacuum results in the formation of fast ions and neutrals with sufficiently high kinetic energies that can form dense films when deposited on a substrate. However, background gas pressures can be used to condense the laser-generated plume resulting in the formation of nanoparticles in the gas-phase. Figure 1b shows the schematic illustration of the plume dynamic as a function of background gas pressures while other parameters (e.g., laser fluence, repetition rate) are kept constants.

To tune the plume condensation dynamics for the formation of nanoparticles, argon gas was used to adjust the background pressure ranging from 0.5 to 5 torr. This pressure range allowed us to create depositions ranging from dense film to mesoporous structures as a function of increasing

pressure. SEM images of room-temperature-deposited structures at different background pressures are shown in Figure 2a-c. The images revealed that at pressures up to 0.5 torr (Figure 2a), mainly dense films are formed on the substrates due to the existence of atoms, molecules, and smaller aggregates in the plume. As the pressure was increased to around 2 torr (Figure 2b), the plume condensed to a semi-sphere of about 5cm in diameter. In this condition, nanoparticles were mainly started forming and creating mesoporous structures as deposited onto the substrates. Increasing the pressure close to 5 torr resulted in the intense condensation of the plume to a semi-sphere of about 1.5 cm in diameter. This high condensation created partially crystallized and sintered agglomeration of nanoparticles, which created loosely connected and fluffier structures when deposited onto the substrates (Figure 2c). It should be noted that pressures beyond 5 torr resulted in small plume sizes that were challenging to bring the substrate close by for deposition. In general, the density and size of the nanoparticle agglomerations were found to be in direct correlation with background pressure due to the condensation effect induced by the background pressure.

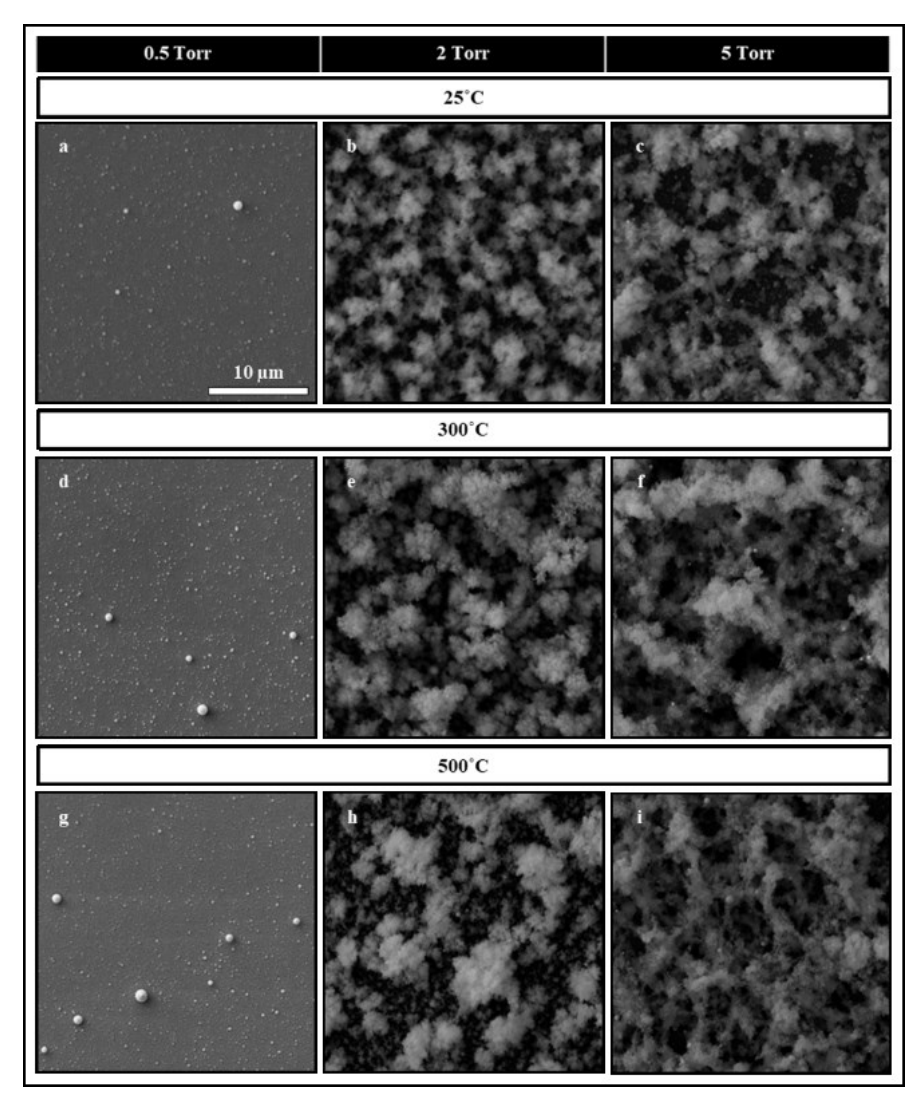


Figure 2. SEM Images of ensemble nanoparticles deposited at 0.5 (a, d and g), 2 (b, e, and h) and 5 torr (c, f, and i). The baking temperature effects on the morphology of the nanoparticles ensembles for different pressure conditions are shown for room-temperature (a, b and c), 300 (d, e and f), and 500 °C (g, h and i). The deposition morphology shows a denser film at 0.5 torr and becomes more mesoporous at higher pressures. Temperature treatments of the samples resulted in the crystallization and sintering of the nanoparticles and the formation of a larger blub of nanoparticles. All images are on the same scale bar.

Following the deposition, nanoparticles were baked at different temperatures aiming reduction of surface traps and studying their behavior under different temperatures. At atmospheric background pressure, a temperature window of 200 to 500 °C was used for baking the nanoparticles in a 3-zone tube furnace for 30 min with continuous argon flow throughout the baking and cooling process to avoid oxidations. The SEM images of nanoparticles deposited at 0.5, 2, and 5 torr and heat-treated at 300 and 500 °C are shown in Figure 2d-i. The SEM images revealed that as the temperature increased, the nanoparticles start sinter together, forming larger agglomerates and pores, as clearly seen in the samples deposited at 2 and 5 torr background pressures. The depositions at 0.5 torr (Figure 2d, g) are nearly continuous dense structures, and their sintering does not reveal significant morphological changes.

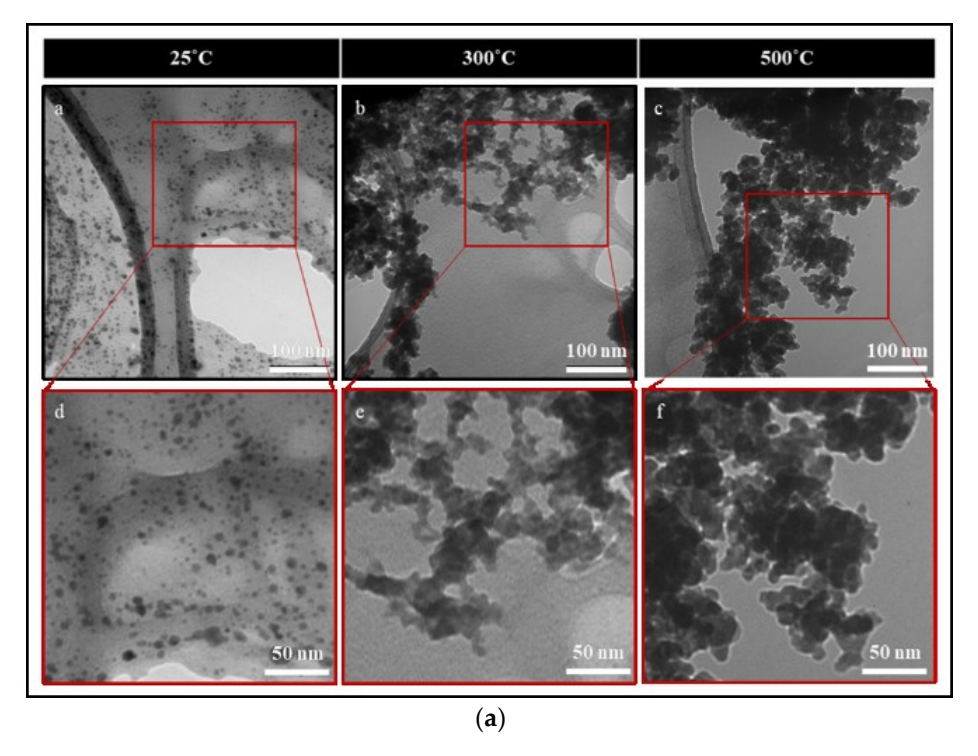


Figure 3. TEM images of the nanoparticles deposited at 2 torr in the as-deposited case (a, d) in addition to the baked cases at 300 °C (b, c) and 500 °C (c, f). The TEM images in the as-deposited case are well separated. However, the particles are sintering at higher temperatures.

As shown in Figure 3, TEM imaging was used to directly observe the nanoparticle size and structural evolution of nanoparticles deposited at 2 torr and under different crystallization temperatures. Samples were sonicated in ethanol and captured onto TEM grids for imaging. The room-temperature deposited samples were easily separated from each other, and individual nanoparticles of about 5-10 nm in size were collected on the TEM grids (Figure 3a, d). Partial crystallization and sintering of nanoparticles were observed for the samples heat-treated at 300 °C (Figure 3b, e). At 500 °C, further sintering of nanoparticles into larger structures was clearly observed (Figure 3c, f). These observations were consistent with the morphological evolutions observed in the SEM images.

The optical properties of the ensemble nanoparticles were studied to understand the correlation between the PL emission, deposition pressures, and crystallization temperatures. The PL spectroscopy was performed using a 405 nm picosecond laser as an excitation source. The laser power was minimized to avoid any photo-induced damage, crystallization, sintering, or oxidation of the nanoparticles during the optical spectroscopy measurements. Figure 4a-e shows the PL emission of the ensemble nanoparticles formed at different background pressures (0.5, 1, 2, 3, and 5 torr) in the as-deposited case and at the indicated crystallization/sintering temperatures (200, 300, 400 and 500 °C for 30 minutes). For the ease of observation, these data are also replotted in Figure 5a-e to show

185

186

187

188

189

190

191

192

193

194

195

196

197

198

199

200

201

202

203

204

205

206

207

208

209

210

the crystallization/sintering temperature effect at 0.5, 1, 2, 3, and 5 torr. The PL spectra were also obtained and analyzed using a continuous-wave 532 nm laser (see Supporting Information).

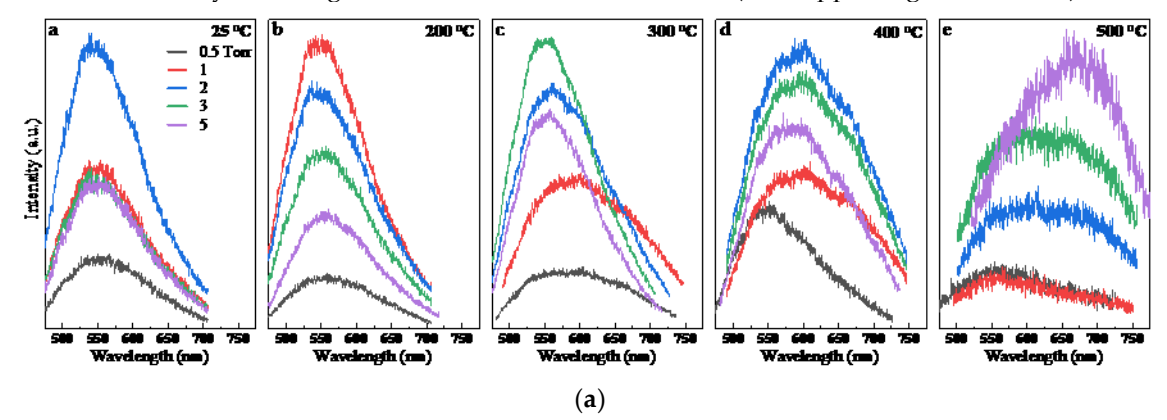


Figure 4. PL spectra of the nanoparticles deposited at various pressure for the as-deposited case (a) and at the indicated baking temperatures (b-e). The sample deposited at 0.5 torr shows the weakest PL emission for all due to the formation of dense films (i.e., no nanoparticles). The PL spectra at 2, 3, and 5 torr have the maximum intensities due to the formation of nanoparticles.

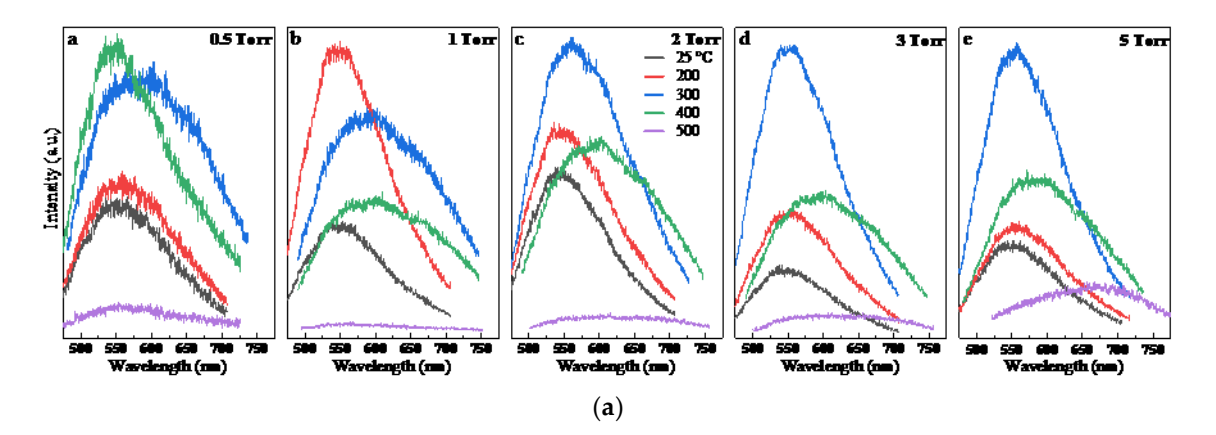


Figure 5. PL spectra showing the effect of baking temperature on the nanoparticles deposited at the indicated pressures (a-e). As the temperate raises to a suitable baking temperature of ~200-300 °C, nanoparticles emission increases largely, and at higher temperatures (i.e., 500 °C) the intensity reduces again due to sintering and formation of larger particles.

Three interesting phenomena were observed while studying the effect of pressures and temperatures on the PL properties of the deposited nanoparticles. First, we observed a strong PL emission from the room-temperature-deposited amorphous nanoparticle (Figure 4a), exhibiting a significant blue-shifted emission of ~540 nm compared to the bulk GaSe crystal central emission of ~625 nm (for more information about central emission and FWHM values check tables S1 and S2). In these room-temperature-deposited samples, the PL emission of the samples at 0.5 torr had the weakest intensity of all due to the formation of a dense film on the substrates. The PL intensity increased for nanoparticles deposited at higher pressures, with 2 torr exhibiting the maximum intensity. Second, we observed strong PL enhancements with minimal FWHM widenings by increasing the baking temperatures up to 300 °C (Figure 4b, c). At higher temperatures (Figure 4d, e), the PL intensity was then severely dropped, FWHM was broadened, and the central emission redshifted toward the emission of bulk crystal and beyond. Third, the lower pressure deposited samples experienced red-shifting and broadening at a lower temperature than high pressure deposited samples. For instance, at 200 °C (Figure 4b), the samples deposited at 1 and 2 torr showed the highest intensity values compared to other pressures. In addition, they had the most blue-shifted emissions and lowest FWHM values. At 300 °C (Figure 4c), the nanoparticles deposited at 2, 3, and 5 torr showed higher intensities, minimal broadening and red-shift. At 400 and 500 °C (Figure 4d, e), significant

211

220

226

227

228

229

230

231

232

233

234

235

236

emission broadening, red-shift, and reduction in the intensities are observed (as seen from the noisy spectra). The low pressure deposited samples (i.e., 0.5 and 1 torr), which were more like thin films rather than nanoparticles, appeared unstable at higher temperatures (e.g., 400-500 °C) as they revealed random changes in their optical properties.

To better observe the effect of baking temperatures on the PL emission characteristics, the temperature effects were plotted for nanoparticles deposited at each background pressure (Figure 5). For 2, 3, and 5 torr samples (Figure 5c, d, and e), a slight red-shift is observed. However, the intensity continued increasing, reaching its maximum at ~300 °C, but this was followed by the steady dropping of the intensity values. The intensity enhancement suggests that heat treatments lead to the crystallization of nanoparticles and the reduction of defects. The FWHMs slight widening and the red-shifting effect could be due to the formation of larger particles as they slowly sinter together at low temperatures (i.e., 200 and 300 °C). However, the sintering effect at the higher temperatures (i.e., 400 and 500 °C) could create nanoparticles with random size distributions as well as degradation and formation of defects in the structures. Such analyses are still primary, and further investigations are needed to fully understand the fundamental mechanisms governing such behaviors.

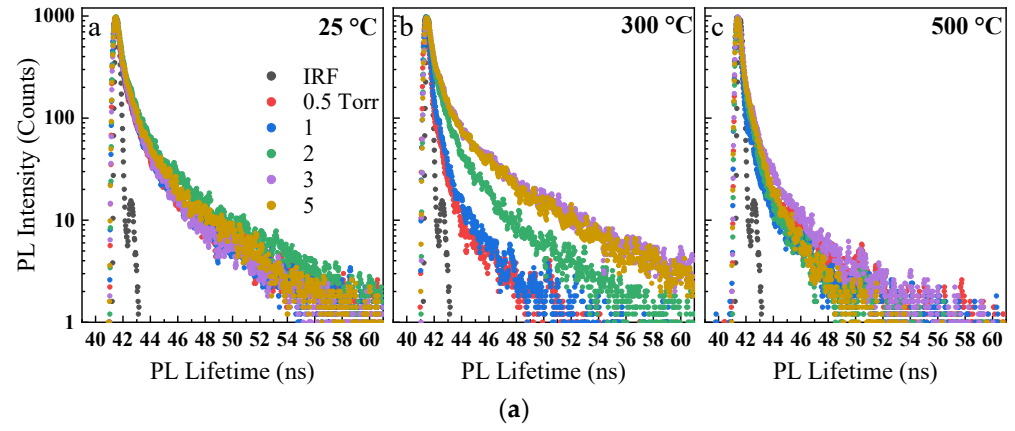


Figure 6. PL lifetime of the nanoparticles deposited at various pressure and heat-treated at different temperatures, including the as-deposited (a), 300 °C (b), and 500 °C (c). The overall trend shows that the PL lifetime increases as the deposition pressure increases.

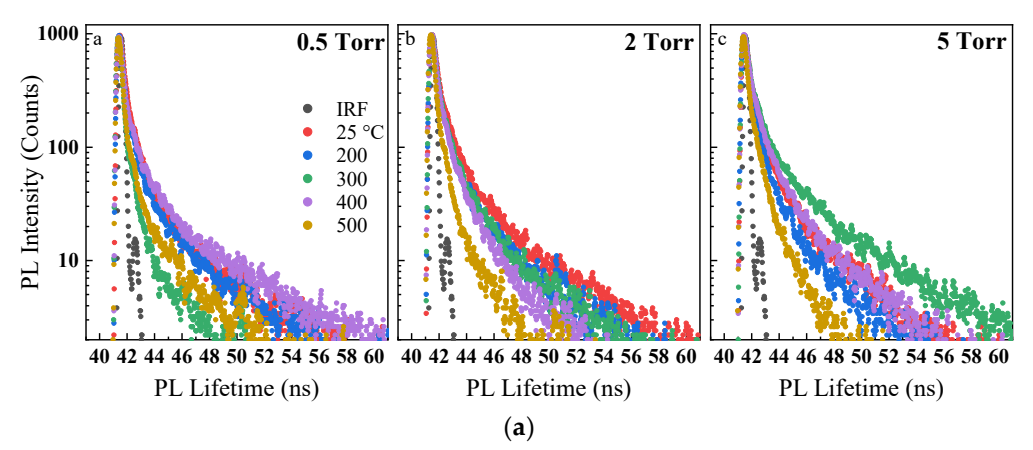


Figure 7. PL lifetime showing the effect of baking temperature on the nanoparticles deposited at the indicated pressure (a, b, and c). The overall trend shows that the PL lifetime decreases as the baking temperature increases.

The PL lifetime of the synthesized nanoparticles was obtained using a time-correlated singlephoton counting (TCSPC) instrument. The measurements were performed using a picosecond 405 nm excitation source. The curves were fitted using EzTime software, and tri-exponential function and characteristic lifetimes were obtained (see Supporting Information). In general, the lifetime of all samples was less than 0.4 ns compared to the 1 ns lifetime of the bulk GaSe crystal. According to the

measurements, the average lifetime of the room-temperature deposited samples (Figure 6a) gradually increased up to 2 torr and then slightly decreased afterward. At 300 °C (Figure 6b), lifetime was found to be positively correlated to the deposition background pressure. In general, it could be inferred that partial crystallization of nanoparticles and hence reduction of the defects are occurring inside the laser-plasma at higher deposition pressures. As for the nanoparticles baked at 500 °C (Figure 6c), the lifetimes decreased again due to possible defect formation at this temperature, similar to the PL emission behaviors.

To better observe the effect of baking temperatures on the PL lifetime of the samples, the temperature effects were plotted for nanoparticles deposited at each background pressure (e.g., 0.5, 2, and 5 torr) (Figure 7). For instance, the average lifetime of the samples deposited at 2 torr (Figure 7b) noticeably reduced from 0.388 ns for the room-temperature-deposited nanoparticles to 0.29 ns at 200 °C. The average lifetime was almost equal for 200 °C and 300 °C and then decreased slowly to 0.138 ns when baked at 500 °C. This agrees well with the red-shift and broadening of 2 torr PL, indicating increased crystallization and moderate sintering of the nanoparticles at low baking temperatures and formation of new defects as the temperature increases. For the sample deposited at 0.5 torr (Figure 7a), the average lifetime decreased up to 300 °C, similar to the 2 torr sample. However, it increased again at ~400 °C. For the samples deposited at 5 torr (Figure 7c), the average lifetime decreased from 0.374 ns for the room-temperature-deposited nanoparticles to 0.266 ns the nanoparticles baked at 200 °C. The lifetime then increased again at ~300 °C, and gradually reduced up to 500 °C. This behavior was again in agreement with our previous PL emission behavior and analyses. In general, the samples tend to crystalize and minimize their defect density when baked up to certain temperatures (i.e., ~300 °C), and at higher temperatures (i.e., 400 and 500 °C) new temperature-induced degradation and defects are further formed. This model is similar to the model proposed by Fassl et al.[58] on MAPbI₃ perovskite films. Such initial room-temperature analyses open the way for more studies on the effect of surface and deep defects on optical properties of GaSe and other 2D nanoparticles in solution-less conditions.

According to the PL emission and lifetime results, samples prepared at 2 torr background pressure showed the optimum optical properties. The crystallization of these nanoparticles at 200-300 °C significantly increased their emission intensity with reduced FWHM. Therefore, the baking time dependence of the PL emission and PL lifetime of the nanoparticles deposited at 2 torr was further studied by heating them at 300 °C for 1, 15, 30, and 120 min to understand the effect of baking time. As shown, a significant increase in the PL intensity was observed by increasing the baking time (figure 6a). In addition, the average PL lifetime decreased from about 0.4 ns for 1min to 0.25 ns for 30 minutes of baking time, respectively (figure 6b). However, with longer baking time (i.e., 120 min), the lifetime increased to 0.4 ns. This outcome confirms the competition between crystallization and sintering during the heat treatments, as also seen in the above PL data.

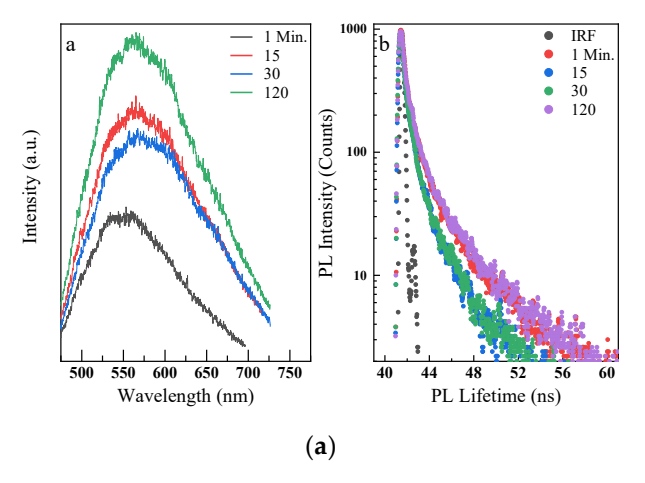


Figure 8. Baking time effect on the nanoparticles deposited at 2 torr and baked at 300 °C. PL spectra increase as the baking time increases (a). This is possibly due to defects-reduction. The average PL lifetime decreases up to 30 min baking time and then increases at 120 min (b).

276 4. Conclusion

277

278

279

280

281

282

283

284

285

286

287

288

289

299

300

In summary, 2D GaSe nanoparticle ensembles mimicking the quantum dots behaviors can be formed in the gas-phase by precisely tuning the nonequilibrium environment in the laser ablation process. Room temperature deposition of these nanoparticles results in the formation of amorphous nanoparticle ensembles on the substrates that can be post-crystallized or sintered. A strong PL can be observed from the amorphous nanoparticles deposited at background pressures. As the baking temperature increases, the nanoparticles tend to crystallize and reduce their defects, leading to the enhanced PL intensities and longer lifetimes. However, increasing the temperatures beyond a threshold results in sintering these nanoparticles together, forming bigger structures, generating new defects, or inducing a phase change that could alter the PL emission intensities, central frequency, and lifetime. This nonequilibrium gas-phase method allows us to investigate the formation of other 2D nanoparticles and explore the new properties emerging from such 2D quantum dot-like structures. In addition, this method allows the formation of designed heterostructures among various 2D nanoparticles.

- Author Contributions: S.E. contributed to the experimental design, materials characterization, data analysis, and manuscript preparation. Z.A. and N.A. helped with data analysis and participated in manuscript preparation. M.M.S. led the project, participated in experimental design, data acquisition and analysis, discussions, and manuscript preparation. All authors have read and agreed to the published version of the manuscript.
- Funding: This research was partially funded by the U.S. National Science Foundation (NSF) under grant No. 1923363.
- Acknowledgments: The authors would like to thank Alabama Micro/Nanoelectronic Science and Technology
 Center (AMNSTC) for providing access to the cleanroom facility.

References

- 301 1. Ahmadi, Z.; Yakupoglu, B.; Azam, N.; Elafandi, S.; Mahjouri-Samani, M., Application of lasers in the synthesis and processing of two-dimensional quantum materials. Journal of Laser Applications 2019, 31 303
- Bhimanapati, G. R.; Lin, Z.; Meunier, V.; Jung, Y.; Cha, J.; Das, S.; Xiao, D.; Son, Y.; Strano, M. S.; Cooper,
 V. R.; Liang, L.; Louie, S. G.; Ringe, E.; Zhou, W.; Kim, S. S.; Naik, R. R.; Sumpter, B. G.; Terrones, H.; Xia,
 F.; Wang, Y.; Zhu, J.; Akinwande, D.; Alem, N.; Schuller, J. A.; Schaak, R. E.; Terrones, M.; Robinson, J. A.,
 Recent Advances in Two-Dimensional Materials beyond Graphene. ACS Nano 2015, 9 (12), 11509-11539.
- 308 3. Gupta, A.; Sakthivel, T.; Seal, S., Recent development in 2D materials beyond graphene. Prog Mater Sci 2015, 73, 44-126.
- Wang, X.; Sun, G.; Li, N.; Chen, P., Quantum dots derived from two-dimensional materials and their applications for catalysis and energy. Chemical Society Reviews 2016, 45 (8), 2239-2262.
- 5. Gao, M.-R.; Xu, Y.-F.; Jiang, J.; Yu, S.-H., Nanostructured metal chalcogenides: synthesis, modification, and applications in energy conversion and storage devices. Chemical Society Reviews 2013, 42 (7).
- 314 6. Azam, N.; Ahmadi, Z.; Yakupoglu, B.; Elafandi, S.; Tian, M.; Boulesbaa, A.; Mahjouri-Samani, M., Accelerated synthesis of atomically-thin 2D quantum materials by a novel laser-assisted synthesis technique. 2D Materials 2019, 7 (1).
- Ahmadi, Z.; Yakupoglu, B.; Azam, N.; Elafandi, S.; Mahjouri-Samani, M., Self-limiting laser crystallization and direct writing of 2D materials. International Journal of Extreme Manufacturing 2019, 1 (1).
- 8. Kumar, A.; Ahluwalia, P. K., Electronic structure of transition metal dichalcogenides monolayers 1H-MX2 (M = Mo, W; X = S, Se, Te) from ab-initio theory: new direct band gap semiconductors. The European Physical Journal B 2012, 85 (6).
- Stanford, M. G.; Pudasaini, P. R.; Gallmeier, E. T.; Cross, N.; Liang, L.; Oyedele, A.; Duscher, G.; Mahjouri Samani, M.; Wang, K.; Xiao, K.; Geohegan, D. B.; Belianinov, A.; Sumpter, B. G.; Rack, P. D., High
 Conduction Hopping Behavior Induced in Transition Metal Dichalcogenides by Percolating Defect
 Networks: Toward Atomically Thin Circuits. Advanced Functional Materials 2017, 27 (36).

- 326 10. Ye, L.; Li, H.; Chen, Z.; Xu, J., Near-Infrared Photodetector Based on MoS2/Black Phosphorus Heterojunction. ACS Photonics 2016, 3 (4), 692-699.
- 328 11. Fu, Q.; Yang, L.; Wang, W.; Han, A.; Huang, J.; Du, P.; Fan, Z.; Zhang, J.; Xiang, B., Synthesis and Enhanced Electrochemical Catalytic Performance of Monolayer WS2(1-x)Se2xwith a Tunable Band Gap. Advanced Materials 2015, 27 (32), 4732-4738.
- 12. Morell, N.; Reserbat-Plantey, A.; Tsioutsios, I.; Schädler, K. G.; Dubin, F.; Koppens, F. H. L.; Bachtold,
 A., High Quality Factor Mechanical Resonators Based on WSe2 Monolayers. Nano Letters 2016, 16 (8), 5102-5108.
- 334 13. Butler, S. Z.; Hollen, S. M.; Cao, L.; Cui, Y.; Gupta, J. A.; Gutiérrez, H. R.; Heinz, T. F.; Hong, S. S.; Huang, J.; Ismach, A. F.; Johnston-Halperin, E.; Kuno, M.; Plashnitsa, V. V.; Robinson, R. D.; Ruoff, R. S.; Salahuddin, S.; Shan, J.; Shi, L.; Spencer, M. G.; Terrones, M.; Windl, W.; Goldberger, J. E., Progress, Challenges, and Opportunities in Two-Dimensional Materials Beyond Graphene. ACS Nano 2013, 7 (4),
- 338 2898-2926.
- 339 14. Ahmed, S.; Yi, J., Two-Dimensional Transition Metal Dichalcogenides and Their Charge Carrier Mobilities in Field-Effect Transistors. Nano-Micro Letters 2017, 9 (4).
- 15. 15. Chhowalla, M.; Shin, H. S.; Eda, G.; Li, L.-J.; Loh, K. P.; Zhang, H., The chemistry of two-dimensional layered transition metal dichalcogenide nanosheets. Nature Chemistry 2013, 5 (4), 263-275.
- 343 16. Desai, S. B.; Madhvapathy, S. R.; Sachid, A. B.; Llinas, J. P.; Wang, Q.; Ahn, G. H.; Pitner, G.; Kim, M. J.; Bokor, J.; Hu, C.; Wong, H. S. P.; Javey, A., MoS2 transistors with 1-nanometer gate lengths. Science 2016, 354 (6308), 99-102.
- Wang, Q. H.; Kalantar-Zadeh, K.; Kis, A.; Coleman, J. N.; Strano, M. S., Electronics and optoelectronics of two-dimensional transition metal dichalcogenides. Nature Nanotechnology 2012, 7 (11), 699-712.
- 348 18. Bae, S.-H.; Kum, H.; Kong, W.; Kim, Y.; Choi, C.; Lee, B.; Lin, P.; Park, Y.; Kim, J., Integration of bulk materials with two-dimensional materials for physical coupling and applications. Nature Materials 2019, 18 (6), 550-560.
- 351 19. Wang, Y.; Liu, Y.; Zhang, J.; Wu, J.; Xu, H.; Wen, X.; Zhang, X.; Tiwary, C. S.; Yang, W.; Vajtai, R.; Zhang, 352 Y.; Chopra, N.; Odeh, I. N.; Wu, Y.; Ajayan, P. M., Cryo-mediated exfoliation and fracturing of layered materials into 2D quantum dots. Science Advances 2017, 3 (12).
- 354 20. Huang, H.; Du, C.; Shi, H.; Feng, X.; Li, J.; Tan, Y.; Song, W., Water-Soluble Monolayer Molybdenum Disulfide Quantum Dots with Upconversion Fluorescence. Particle & Particle Systems Characterization 2015, 32 (1), 72-79.
- 21. Liu, Y.; Liang, C.; Wu, J.; Varma, S. J.; Nakanishi, Y.; Aliyan, A.; Martí, A. A.; Wang, Y.; Xie, B.; Kumar, J.; Layne, K.; Chopra, N.; Odeh, I.; Vajtai, R.; Thomas, J.; Peng, X.; Yang, W.; Ajayan, P. M., Reflux pretreatment-mediated sonication: A new universal route to obtain 2D quantum dots. Materials Today 2019, 22, 17-24.
- 361 22. Xu, Q.; Cai, W.; Li, W.; Sreeprasad, T. S.; He, Z.; Ong, W.-J.; Li, N., Two-dimensional quantum dots: Fundamentals, photoluminescence mechanism and their energy and environmental applications. Materials Today Energy 2018, 10, 222-240.
- 23. Li, B. L.; Setyawati, M. I.; Zou, H. L.; Dong, J. X.; Luo, H. Q.; Li, N. B.; Leong, D. T., Emerging 0D Transition-Metal Dichalcogenides for Sensors, Biomedicine, and Clean Energy. Small 2017, 13 (31).
- 24. Ding, X.; Peng, F.; Zhou, J.; Gong, W.; Slaven, G.; Loh, K. P.; Lim, C. T.; Leong, D. T., Defect engineered bioactive transition metals dichalcogenides quantum dots. Nature Communications 2019, 10 (1).
- Samadi, M.; Sarikhani, N.; Zirak, M.; Zhang, H.; Zhang, H.-L.; Moshfegh, A. Z., Group 6 transition metal
 dichalcogenide nanomaterials: synthesis, applications and future perspectives. Nanoscale Horizons 2018,
 3(2), 90-204.
- Yang, L.; Xie, C.; Jin, J.; Ali, R.; Feng, C.; Liu, P.; Xiang, B., Properties, Preparation and Applications of Low
 Dimensional Transition Metal Dichalcogenides. Nanomaterials 2018, 8 (7).
- Wang, Y.; Ni, Y., Molybdenum Disulfide Quantum Dots as a Photoluminescence Sensing Platform for 2,4,6 Trinitrophenol Detection. Analytical Chemistry 2014, 86 (15), 7463-7470.
- 375 28. Gu, W.; Yan, Y.; Zhang, C.; Ding, C.; Xian, Y., One-Step Synthesis of Water-Soluble MoS2Quantum Dots via a Hydrothermal Method as a Fluorescent Probe for Hyaluronidase Detection. ACS Applied Materials & Interfaces 2016, 8 (18), 11272-11279.

- 29. Dong, H.; Tang, S.; Hao, Y.; Yu, H.; Dai, W.; Zhao, G.; Cao, Y.; Lu, H.; Zhang, X.; Ju, H., Fluorescent MoS2
 Quantum Dots: Ultrasonic Preparation, Up-Conversion and Down-Conversion Bioimaging, and
 Photodynamic Therapy. ACS Applied Materials & Interfaces 2016, 8 (5), 3107-3114.
- 381 30. Zhang, S.; Jia, X.; Wang, E., Facile synthesis of optical pH-sensitive molybdenum disulfide quantum dots. Nanoscale 2016, 8 (33), 15152-15157.
- 383 31. Dhanabalan, S. C.; Dhanabalan, B.; Ponraj, J. S.; Bao, Q.; Zhang, H., 2D-Materials-Based Quantum Dots: Gateway Towards Next-Generation Optical Devices. Advanced Optical Materials 2017, 5 (19).
- 385 32. Zhang, S.; Liu, X.; Liu, C.; Luo, S.; Wang, L.; Cai, T.; Zeng, Y.; Yuan, J.; Dong, W.; Pei, Y.; Liu, Y., MoS2
 386 Quantum Dot Growth Induced by S Vacancies in a ZnIn2S4 Monolayer: Atomic-Level Heterostructure for
 387 Photocatalytic Hydrogen Production. ACS Nano 2017, 12 (1), 751-758.
- 388 33. Ghorai, A.; Bayan, S.; Gogurla, N.; Midya, A.; Ray, S. K., Highly Luminescent WS2 Quantum Dots/ZnO Heterojunctions for Light Emitting Devices. ACS Applied Materials & Interfaces 2016, 9 (1), 558-565.
- 390 34. Ibrahim, K. H.; Irannejad, M.; Wales, B.; Sanderson, J.; Yavuz, M.; Musselman, K. P., Simultaneous Fabrication and Functionalization of Nanoparticles of 2D Materials with Hybrid Optical Properties. Advanced Optical Materials 2018, 6 (11).
- 393 35. Caigas, S. P.; Cheng, M.-C.; Lin, T.-N.; Santiago, S. R. M. S.; Yuan, C.-T.; Yang, C.-C.; Chou, W.-C.; Shen, J.-L., P-Type Doping of WS2 Quantum Dots via Pulsed Laser Ablation. ACS Photonics 2018, 5 (12), 4828-4837.
- 395 36. Lin, L.; Xu, Y.; Zhang, S.; Ross, I. M.; Ong, A. C. M.; Allwood, D. A., Fabrication of Luminescent Monolayered Tungsten Dichalcogenides Quantum Dots with Giant Spin-Valley Coupling. ACS Nano 2013, 7 (9), 8214-8223.
- 37. Vikraman, D.; Akbar, K.; Hussain, S.; Yoo, G.; Jang, J.-Y.; Chun, S.-H.; Jung, J.; Park, H. J., Direct synthesis of thickness-tunable MoS2 quantum dot thin layers: Optical, structural and electrical properties and their application to hydrogen evolution. Nano Energy 2017, 35, 101-114.
- 401 38. Gopalakrishnan, D.; Damien, D.; Shaijumon, M. M., MoS2 Quantum Dot-Interspersed Exfoliated MoS2 Nanosheets. ACS Nano 2014, 8 (5), 5297-5303.
- 403 39. Štengl, V.; Henych, J., Strongly luminescent monolayered MoS2 prepared by effective ultrasound exfoliation. Nanoscale 2013, 5 (8).
- 40. Yan, Y.; Zhang, C.; Gu, W.; Ding, C.; Li, X.; Xian, Y., Facile Synthesis of Water-Soluble WS2 Quantum Dots for Turn-On Fluorescent Measurement of Lipoic Acid. The Journal of Physical Chemistry C 2016, 120 (22), 12170-12177.
- 408 41. Xu, S.; Li, D.; Wu, P., One-Pot, Facile, and Versatile Synthesis of Monolayer MoS2/WS2Quantum Dots as Bioimaging Probes and Efficient Electrocatalysts for Hydrogen Evolution Reaction. Advanced Functional Materials 2015, 25 (7), 1127-1136.
- 411 42. Xu, Y.; Wang, X.; Zhang, W. L.; Lv, F.; Guo, S., Recent progress in two-dimensional inorganic quantum dots. Chemical Society Reviews 2018, 47 (2), 586-625.
- 413 43. Ou, G.; Fan, P.; Ke, X.; Xu, Y.; Huang, K.; Wei, H.; Yu, W.; Zhang, H.; Zhong, M.; Wu, H.; Li, Y., Defective molybdenum sulfide quantum dots as highly active hydrogen evolution electrocatalysts. Nano Research 2017, 11 (2), 751-761.
- 416 44. Xu, Y.; Yan, L.; Li, X.; Xu, H., Fabrication of transition metal dichalcogenides quantum dots based on femtosecond laser ablation. Scientific Reports 2019, 9 (1).
- 418 45. Li, B.; Jiang, L.; Li, X.; Ran, P.; Zuo, P.; Wang, A.; Qu, L.; Zhao, Y.; Cheng, Z.; Lu, Y., Preparation of Monolayer MoS2 Quantum Dots using Temporally Shaped Femtosecond Laser Ablation of Bulk MoS2 Targets in Water. Scientific Reports 2017, 7 (1).
- 421 46. Qiao, W.; Yan, S.; Song, X.; Zhang, X.; He, X.; Zhong, W.; Du, Y., Luminescent monolayer MoS2 quantum dots produced by multi-exfoliation based on lithium intercalation. Applied Surface Science 2015, 359, 130-136.
- 424 47. Cao, X.; Ding, C.; Zhang, C.; Gu, W.; Yan, Y.; Shi, X.; Xian, Y., Transition metal dichalcogenide quantum dots: synthesis, photoluminescence and biological applications. Journal of Materials Chemistry B 2018, 6 (48), 8011-8036.
- 427 48. Zhang, X.; Cheng, H.; Zhang, H., Recent Progress in the Preparation, Assembly, Transformation, and Applications of Layer-Structured Nanodisks beyond Graphene. Advanced Materials 2017, 29 (35).
- 429 49. Valappil, M. O.; Anil, A.; Shaijumon, M.; Pillai, V. K.; Alwarappan, S., A Single-Step Electrochemical Synthesis of Luminescent WS2 Quantum Dots. Chemistry A European Journal 2017, 23 (38), 9144-9148.

- 431 50. Gopalakrishnan, D.; Damien, D.; Li, B.; Gullappalli, H.; Pillai, V. K.; Ajayan, P. M.; Shaijumon, M. M., Electrochemical synthesis of luminescent MoS2 quantum dots. Chemical Communications 2015, 51 (29), 6293-6296.
- 434 51. Mahjouri-Samani, M.; Gresback, R.; Tian, M.; Wang, K.; Puretzky, A. A.; Rouleau, C. M.; Eres, G.; Ivanov, 435 I. N.; Xiao, K.; McGuire, M. A.; Duscher, G.; Geohegan, D. B., Pulsed Laser Deposition of Photoresponsive Two-Dimensional GaSe Nanosheet Networks. Advanced Functional Materials 2014, 24 (40), 6365-6371.
- 437 52. Stoll, S. L.; Gillan, E. G.; Barron, A. R., Chemical vapor deposition of Gallium selenide nanoparticles. Chemical Vapor Deposition 1996, 2 (5), 182-184.
- 439 53. Allakhverdiev, K.; Hagen, J.; Salaeva, Z., On a Possibility to Form Small Crystallites of Layered Gallium Selenide via Ultrasonic Treatment. physica status solidi (a) 1997, 163 (1), 121-127.
- 54. Chikan, V.; Kelley, D. F., Synthesis of Highly Luminescent GaSe Nanoparticles. Nano Letters 2002, 2 (2), 141-145.
- 443 55. Mahjouri-Samani, M.; Tian, M.; Puretzky, A. A.; Chi, M.; Wang, K.; Duscher, G.; Rouleau, C. M.; Eres, G.; 444 Yoon, M.; Lasseter, J.; Xiao, K.; Geohegan, D. B., Nonequilibrium Synthesis of TiO2 Nanoparticle "Building Blocks" for Crystal Growth by Sequential Attachment in Pulsed Laser Deposition. Nano Letters 2017, 17 (8), 4624-4633.
 - 56. Mahjouri-Samani, M.; Tian, M.; Wang, K.; Boulesbaa, A.; Rouleau, C. M.; Puretzky, A. A.; McGuire, M. A.; Srijanto, B. R.; Xiao, K.; Eres, G.; Duscher, G.; Geohegan, D. B., Digital Transfer Growth of Patterned 2D Metal Chalcogenides by Confined Nanoparticle Evaporation. ACS Nano 2014, 8 (11), 11567-11575.
 - 57. Dai, Q.; Chen, J.; Lu, L.; Tang, J.; Wang, W., Pulsed Laser Deposition of CdSe Quantum Dots on Zn2SnO4 Nanowires and Their Photovoltaic Applications. Nano Letters 2012, 12 (8), 4187-4193.
 - 58. Fassl, P.; Zakharko, Y.; Falk, L. M.; Goetz, K. P.; Paulus, F.; Taylor, A. D.; Zaumseil, J.; Vaynzof, Y., Effect of density of surface defects on photoluminescence properties in MAPbI3 perovskite films. *Journal of Materials Chemistry C* 2019, 7 (18), 5285-5292.



© 2020 by the authors. Submitted for possible open access publication under the terms and conditions of the Creative Commons Attribution (CC BY) license (http://creativecommons.org/licenses/by/4.0/).

447

448

449

450

451

452

453

454

455

Gas-Phase Formation of Highly Luminescent 2D GaSe Nanoparticle Ensembles in a Nonequilibrium Laser Ablation Process

Salah Elafandi¹, Zabihollah Ahmadi¹, Nurul Azam¹, and Masoud Mahjouri-Samani^{1*}
¹Department of Electrical and Computer Engineering, Auburn University, Auburn, AL, USA
*Address correspondence to mahjouri@auburn.edu

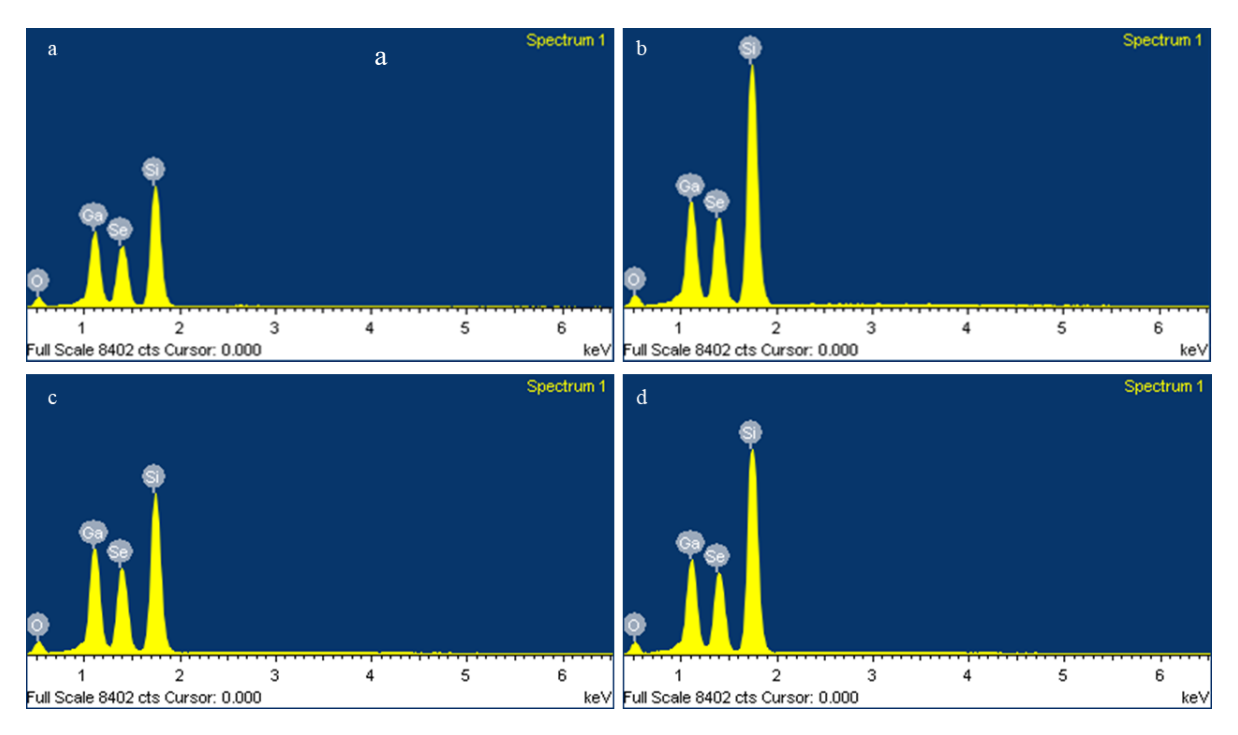


Figure S1. Energy Dispersive X-ray (EDX) results showing the stoichiometry of the as-deposited nanoparticles at 2 torr (**a**) and 5 torr (**b**) background pressures. The results verify that the stoichiometry is maintained even after baking the sample at 400° C (**c,d**).

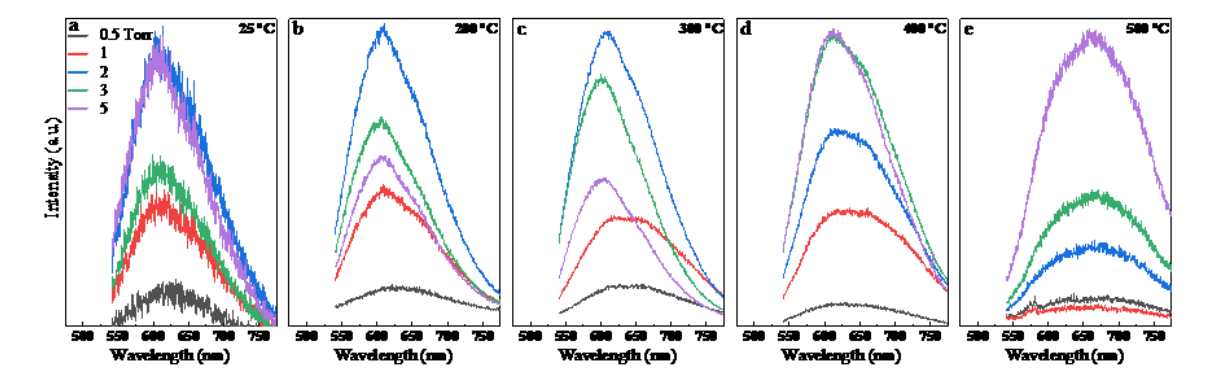


Figure S2. PL spectra of the nanoparticles deposited at various pressures and temperatures (**a-e**), using a 532 nm continuous-wave laser. The sample deposited at 0.5 torr shows the weakest PL emission for all temperatures due to the formation of dense films (i.e., no nanoparticles). The PL spectra of samples deposited at 2, 3 and 5 torr have the maximum intensities due to the formation of nanoparticles.

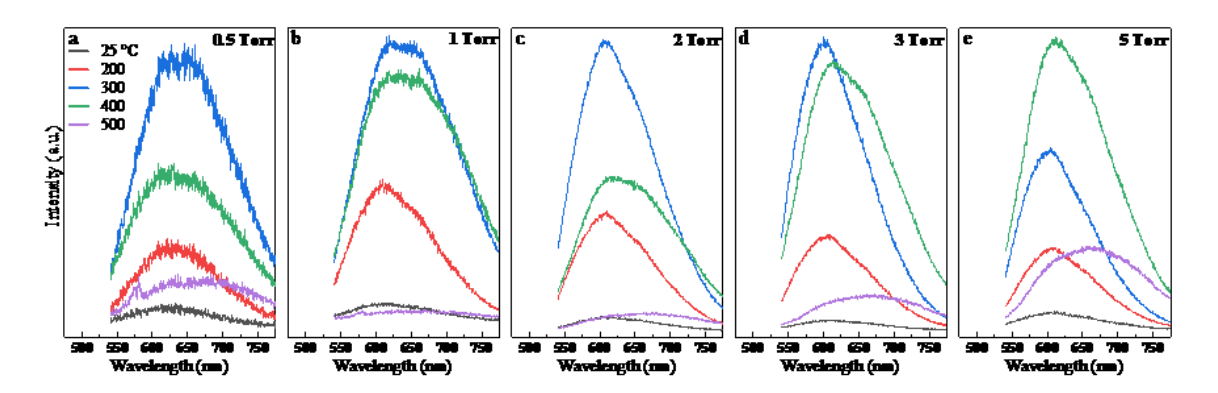


Figure S3. PL spectra showing the effect of baking temperature on the nanoparticles deposited at the indicated pressure (a-e), using a 532 nm continuous-wave laser. Room temperature deposited samples show the weakest emission. As the temperate increases to a suitable crystallization temperature of ~300 °C, nanoparticles emission increases largely, and at higher temperatures (i.e., 500 °C) the intensity reduces again due to sintering and formation of larger particles.

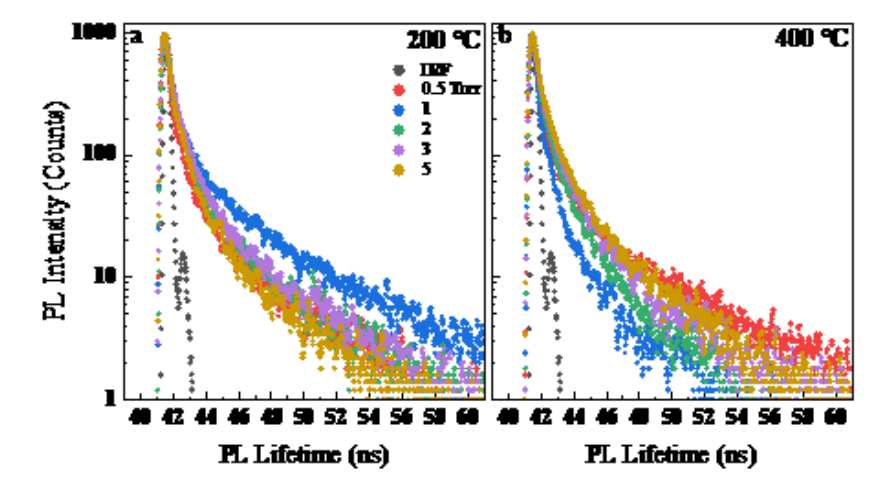


Figure S4. PL lifetime of the nanoparticles deposited at various pressures banked at 200 (a) and 400 °C (b).

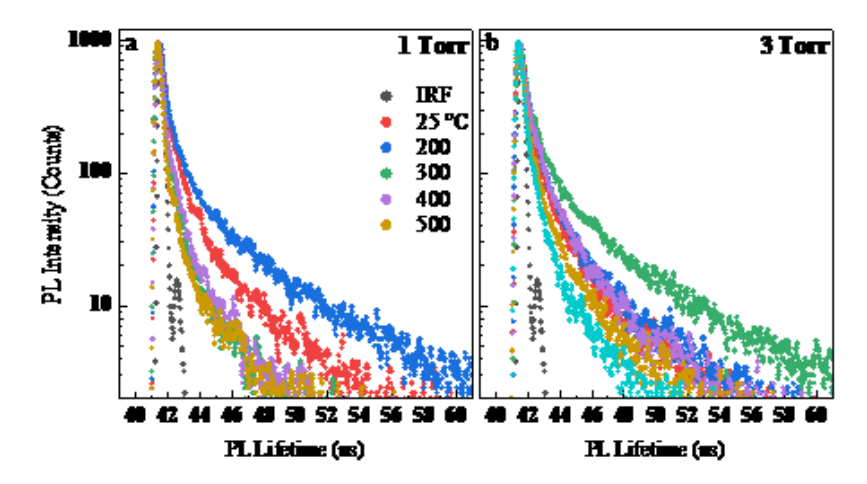


Figure S5. PL lifetime showing the effect of baking temperature on the nanoparticles deposited at 1 (a) and 3 (b) torr.

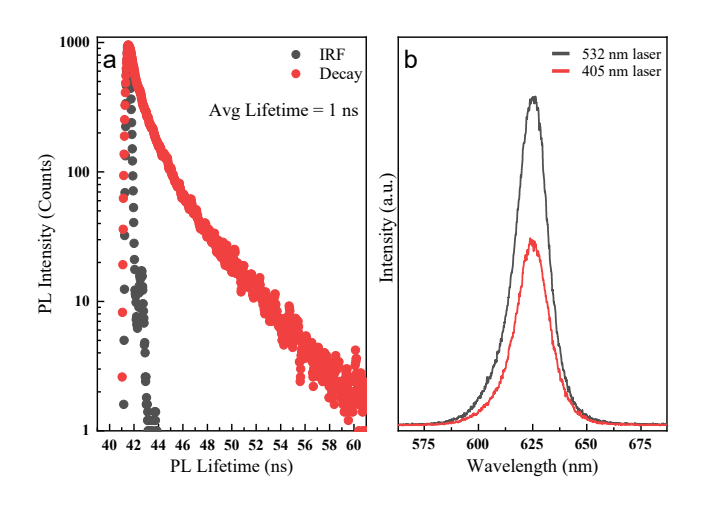


Figure S6. PL lifetime (a) and PL (b) of a bulk GaSe crystal.

Table S1. Central emission values of the PL emission obtained using the picosecond 405 nm laser as an excitation source.

Pressure	Central Emission (nm)	Central Emission (nm)	Central Emission (nm)	Central Emission (nm)	Central Emission (nm)
Temp (°C)	25°C	200°C	300°C	400°C	500°C
0.5	546	549	601	536	546
1	541	541	614	619	547
2	539	539	552	612	630
3	539	544	543	612	631
5	542	548	547	570	674

Table S2. FWHM values of the PL emission obtained using the picosecond 405 nm laser as an excitation source.

Pressure	FWHM	FWHM FWHM		FWHM	FWHM	
	(nm)	(nm)	(nm)	(nm)	(nm)	
Temp (°C)	25°C	200°C	300°C	400°C	500°C	
0.5	129	142.1	208	119	123	
1	110	111	233	227	130	
2	109	118	144	226	235	
3	112	119	116	219	235	
5	111	120	116	189	257	

Table S3. Central emission values of the PL emission obtained using the 532 nm continuous laser as an excitation source.

Pressure (T)	Central Emission (nm)	Central Emission (nm)	Central Emission (nm)	Central Emission (nm)	Central Emission (nm)
Temp (°C)	25°C	200°C	300°C	400°C	500°C
0.5	619	625	631	643	661
1	607	607	626	651	657
2	605	603	603	641	671
3	604	598	594	612	670
5	602	601	595	608	667

Table S4. FWHM values of the PL emission obtained using the 532 nm continuous laser as an excitation source.

Pressure (T)	FWHM (nm)	FWHM (nm)	FWHM (nm)	FWHM (nm)	FWHM (nm)
Temp (°C)	25°C	200°C	300°C	400°C	500°C
0.5	119	118	143	167	173
1	122	119	156	169	159
2	117	113	116	151	201
3	114	108	105	136	185
5	111	106	103	124	177

Table S5. Lifetime fitting parameters of the nanoparticles deposited at 0.5 torr.

	$^{\circ}C$	A	T1 (ns)	T2 (ns)	T3 (ns)	B1	B2	В3	Avg T (ns)
	25	0.3765	0.731225	0.129307	3.627073	0.033445	0.205506	0.003596	0.264171
	200	0.30215	0.588688	3.41839	0.091332	0.032011	0.003651	0.290323	0.177437
5 To	300	0.184215	0.078943	0.478933	2.884721	0.36545	0.024806	0.0011	0.112183
orr	400	0.465397	0.725004	4.066824	0.090214	0.027162	0.004158	0.298196	0.192724
	500	0.63646	0.410023	0.059662	2.369051	0.030851	0.442596	0.003301	0.098325

Table S6. Lifetime fitting parameters of the nanoparticles deposited at 1 torr.

	$^{\circ}\mathbf{C}$	A	T1 (ns)	T2 (ns)	T3 (ns)	B 1	B2	В3	Avg T (ns)
	25	0.4274271	0.7540962	0.1585956	3.2313438	0.032112	0.1708399	0.0042126	0.313385
1	200	0.3543137	0.7101392	4.3855397	0.1132297	0.0383503	0.0065988	0.2031747	0.31911
Torr	300	0.2901749	0.5743158	0.1017695	2.5332397	0.0242911	0.289314	0.0017508	0.151668
Η.	400	0.3237967	0.5250072	0.0906471	2.1481171	0.0330297	0.3004887	0.0032448	0.153074
	500	0.6234256	0.3056314	1.901737	0.0334506	0.0401633	0.0030453	0.9745709	0.0497813

Table S7. Lifetime fitting parameters of the nanoparticles deposited at 2 torr.

	°C	A	T1 (ns)	T2 (ns)	T3 (ns)	B1	B2	В3	Avg T (ns)
	25	0.1750575	0.8592292	4.024655	0.1634982	0.0361958	0.0050445	0.1581142	0.387522
2	200	0.4279814	0.6497374	0.1295084	3.0860115	0.040692	0.1824145	0.0052144	0.289746
Torr	300	0.4761335	0.6633929	0.1328094	2.8366252	0.0391765	0.1749509	0.0059546	0.300413
- T	400	0.3829398	0.5212455	0.120366	1.9983458	0.0483285	0.1789817	0.0083602	0.269193
	500	0.3363721	0.4745001	0.0835505	2.0378402	0.0377126	0.3200647	0.0025176	0.138127

Table S8. Lifetime fitting parameters of the nanoparticles deposited at 3 torr.

	$^{\circ}\mathrm{C}$	A	T1 (ns)	T2 (ns)	T3 (ns)	B 1	B2	В3	Avg T (ns)
	25	0.2446444	0.8186526	0.1679898	3.5211749	0.0320765	0.1575633	0.0032469	0.332638
3	200	0.2543762	0.155196	0.7887412	3.6735355	0.1481988	0.0402304	0.0041208	0.362862
Torr	300	0.3710518	0.7357355	0.1141849	4.3359261	0.0444039	0.1743323	0.0077847	0.38111
T	400	0.4775388	0.7273778	2.7051167	0.1533387	0.0414428	0.0063572	0.1465101	0.359257
	500	0.5027549	0.4406089	2.1853672	0.0809183	0.0506979	0.0058303	0.2861599	0.169936

Table S9. Lifetime fitting parameters of the nanoparticles deposited at 5 torr.

	°C	A	T1 (ns)	T2 (ns)	T3 (ns)	B1	B2	В3	Avg T (ns)
	25	0.2624931	0.7419071	0.1670818	3.2860058	0.0396093	0.1460485	0.0054006	0.374413
55	200	0.3642784	0.7089714	0.1346335	2.8893663	0.0364951	0.1959548	0.0036873	0.266413
Torr	300	0.4108882	0.7462776	4.1229113	0.1276789	0.0438383	0.0076454	0.1691439	0.389039
T.	400	0.3218829	0.7118832	2.9545632	0.1211159	0.046988	0.0070916	0.1756727	0.329395
	500	0.2602637	0.0923414	0.5211756	1.8048778	0.2468006	0.0406756	0.0043775	0.177794